

RESEARCH ARTICLE OPEN ACCESS

Steady-State Carrier Distribution under Short-Circuit Conditions—Role of Electric Field and Generation Rate Profiles in *homo-pn* Solar Cells

Isshin Sumiyoshi  | Yoshitaro Nose 

Department of Materials Science and Engineering, Kyoto University, Kyoto, Japan

Correspondence: Yoshitaro Nose (nose.yoshitaro.5e@kyoto-u.ac.jp)**Received:** 9 June 2025 | **Revised:** 15 August 2025 | **Accepted:** 25 August 2025**Funding:** JST SPRING, Grant/Award Number: JPMJSP2110; JSPS KAKENHI, Grant/Award Numbers: 23K26432 24KJ1392; Collaborative Research Project of Materials and Structures Laboratory**Keywords:** device simulation | excess carrier | recombination | short circuit | solar cell modeling

ABSTRACT

Short-circuit current density (J_{SC}) represents the maximum extractable current for photovoltaics, and closing the gap to its radiative limit is crucial for advanced and emerging technologies. However, analysis of its losses remains unstructured, because the classical current density expression—proportional to carrier concentration and gradient of quasi-Fermi levels—becomes cumbersome under short-circuit conditions. Most simulations therefore focus on the maximum-power point, leaving no clear framework for pinpointing J_{SC} losses or developing design guidelines. Here, we address this issue using a charge-balance framework, in which the divergence of current density equals the net generation at steady state. This formulation reduces the analysis of J_{SC} to identifying the dominant factors governing the excess carrier distribution under short circuit conditions—an approach that constitutes the main contribution of this work. Systematic SCAPS-1D simulations of *homo-pn* solar cells reveal that this distribution is governed primarily by the internal electric field, rather than the equilibrium carrier concentration, although both drift and diffusion contribute. Analysis using infinitesimal photogeneration slices further shows that each excess carrier distribution consists of a peak at the generation site and tails extending into nongeneration regions, both of which drive recombination. This framework offers a direct, quantitative route for identifying and minimizing J_{SC} losses.

1 | Introduction

Short-circuit current density (J_{SC})—the net flow of photogenerated electrons and holes to opposite contacts—sets the upper limit of extractable current, and therefore, ultimately constrains the open-circuit voltage (V_{OC}) and power conversion efficiency of a solar cell [1–8]. State-of-the-art crystalline-silicon (c-Si) devices already achieve ~94% of the Shockley–Queisser (SQ) limit for J_{SC} owing to heterojunction and passivation advances [9–11]. In contrast, other high-efficiency architectures still fall short. Halide perovskite [12, 13], Cu(In, Ga)Se₂ [14–16], and GaAs [17] achieve approximately 90% or less of their radiative limit, whereas

CdSeTe solar cells now yield about 95% of that limit but still exhibit a notable open-circuit voltage deficit [18, 19]. Emerging absorbers such as kesterite [20–22], Sb₂Se₃ [23], and ZnSnP₂ [24, 25] still offer significant potential for improving short-circuit behavior. Moreover, the J_{SC} values cited above represent only the best-performing devices fabricated to date. Numerous preliminary laboratory-scale cells, even those employing advanced architectures, still exhibit substantially lower J_{SC} . Improving the short-circuit current density in these early-stage devices remains essential, as they often serve as stepping stones toward the next technological breakthrough. Bridging this current-density gap, therefore, requires a fundamental understanding of the factors governing J_{SC} .

This is an open access article under the terms of the [Creative Commons Attribution-NonCommercial License](#), which permits use, distribution and reproduction in any medium, provided the original work is properly cited and is not used for commercial purposes.

© 2025 The Author(s). *Solar RRL* published by Wiley-VCH GmbH.

However, understanding of carrier separation under short-circuit conditions—and thus of the resulting J_{SC} —is still far from complete. Experimentally, J_{SC} is most often analyzed using external quantum efficiency (EQE) measurements. While EQE clearly identifies wavelength-resolved losses, it can only offer general interpretations of their origins (e.g., long-wavelength losses are typically attributed to recombination in deep regions); the precise locations and mechanisms of the recombination losses remain poorly understood. To elucidate the origins of current losses, numerical simulations have instead been employed. In principle, the current density is proportional to the product of the carrier concentration and the gradient of the quasi-Fermi levels, indicating that the current density is determined by simulated distributions of these two quantities [1]. In practice, however, directly comparing the absolute J_{SC} or its losses from those profiles is challenging. Under short-circuit conditions, carrier concentrations can span several orders of magnitude, and the associated quasi-Fermi levels can become highly complex, sometimes even exhibiting extrema, making quantitative interpretation based on those profiles difficult. Consequently, most fundamental studies of carrier separation in solar cells have been conducted not at short circuit but at the maximum-power point [5, 6, 26, 27]. At this operating point, the carriers and quasi-Fermi level distributions are dominated by injected excess carriers due to applied bias voltage. This reduces the spatial variation of both distributions, making interpretation based on the standard current expression more straightforward. However, such distributions no longer reflect the original photogeneration and but instead resemble those in a biased diode. In related fields, more advanced optical-generation simulations have been performed for photodiodes and light-emitting diodes, both of which operate under applied bias, rather than short-circuit conditions. For photovoltaics, quantifying where photocurrent originates and where it is lost under zero-bias conditions remains uniquely important.

Here, we replace the complexity of the commonly used current-density expression with a simple charge-balance scheme: under steady-state conditions, the divergence of the current density equals the net generation, that is, total generation minus total recombination. For a given total generation rate, the spatial profile of recombination rate—and thus J_{SC} —is determined solely by the steady-state carrier distribution, without reference to the quasi-Fermi levels. Therefore, the framework to analyze the absolute value of J_{SC} and its losses can instead be restated as determining how the steady-state carrier concentration profile, under illumination with no external bias voltage, is established and how that profile influences recombination. To date, this aspect has received only limited attention, with just a handful of isolated studies addressing excess-carrier concentrations under true short-circuit conditions [28].

In this study, we investigate the key factors governing the steady-state carrier distribution under short-circuit conditions using SCAPS-1D numerical simulations [29], thereby, paving the way for a charge-balance-based analysis of J_{SC} . To reveal the fundamental mechanisms, we consider a simplified *homo-pn* solar cell incorporating a uniformly distributed carrier trap. Systematic simulations on hypothetical structures—in which the drift driving force is fixed while the diffusion driving force is varied—reveal that under short-circuit conditions the excess carrier distribution is governed primarily by the electric-field

profile, rather than by the equilibrium carrier concentration. Further analysis of local photogeneration profiles shows that the excess carriers consist of (i) a peak located in the generation region and (ii) tails extending into nongenerating regions. Because both the peak and the tail increase the excess carrier density and hence the recombination rate, their suppression is essential for achieving high device performance. Combining these findings leads to the conclusion that, under short-circuit conditions, the spatial concentration of excess carriers in a solar cell is entirely determined by the electric field and photogeneration profiles. Finally, using a more realistic model with an exponential generation profile, we quantitatively examine how variations in electric-field distribution influence the extent of the peak and tail formation. This study provides a fundamental framework for quantifying and analyzing the short-circuit current density and its associated losses under conditions involving complex steady-state carrier distributions by clarifying how the electric field and photogeneration profiles jointly shape the excess carrier distribution.

2 | Governing Equations for Charge Balance

2.1 | Expression of Current Density in a Solar Cell

The electron and hole current densities in a one-dimensional solar cell are described by

$$j_k = qz_k M_k n_k \frac{\partial E_{F,k}}{\partial x} \quad (1)$$

where qz_k is the charge of particle k (electrons e or holes h), q is the elementary charge, M_k is their mobility, n_k is their concentration, and $E_{F,k}$ is the Fermi level (in equilibrium) or quasi-Fermi level (under steady-state conditions). Using the Boltzmann approximation, $E_{F,k}$ can be expressed as:

$$\begin{aligned} E_{F,e} &= E_C + kT \ln \frac{n_e}{N_C} \\ E_{F,h} &= E_V + kT \ln \frac{n_h}{N_V} \end{aligned} \quad (2)$$

where E_C and E_V are levels of the conduction band minimum and valence band maximum, k is the Boltzmann constant, T is the temperature, and N_C and N_V are the effective densities of states for conduction and valence bands, respectively. In the dark, the device is in equilibrium, and Equation (1) reduces to zero because the Fermi levels are spatially flat. Under illumination, however, the photogenerated carriers cause the electron and hole quasi-Fermi levels to split. The resulting gradients are no longer zero, and Equation (1) yields a photocurrent. Because n_k and $E_{F,k}$ are inherently interdependent, and n_k can vary by several orders of magnitude, analyzing the magnitude of j_k while focusing on only one factor, as in many previous studies [5, 30, 31], is insufficient.

To simplify the discussion, we focus here on the charge balance among generation, charge flow, and recombination in a solar cell under steady states, given by

$$g = j + j_d + r \quad (3)$$

with

$$g = q \int G(x) dx \quad (4)$$

$$r = q \int U(x) dx \quad (5)$$

where $G(x)$ and $U(x)$ are the generation and recombination rates, respectively, and $j = j_e + j_h$; and j_d is the diode current density (electron flow toward the *p*-type side or hole flow toward the *n*-type side). Therefore, j can be expressed by

$$j = g - j_d - r \quad (6)$$

The recombination process is determined solely by steady-state carrier concentrations rather than by quasi-Fermi levels. $U(x)$ is generally expressed by

$$U(x) = K(n_e n_h - n'_e n'_h) \quad (7)$$

where K is a coefficient that includes parameters such as the capture cross sections and carrier trap density, n_k and n'_k are the concentrations of k under illuminated and dark conditions, respectively. j_d is expressed by

$$j_d = v_1(n_1 - n'_1) + v_2(n_2 - n'_2) \quad (8)$$

where v_i is the surface recombination velocity at i contact (*p*-type side 1 or *n*-type 2), and n_i and n'_i are the minority carrier concentration at i contact under illuminated and the dark, respectively. Because both r and j_d can be determined solely by the carrier concentration, the current density in a system with a known g can be estimated from the carrier distribution based on the charge balance [32]. In this context, what characterizes the carrier distribution would be regarded as the underlying mechanism for carrier separation in a solar cell under short-circuit conditions.

2.2 | Transition Immediately after Illumination to the Steady State

Solar cell operation is inherently in a steady state; therefore, we analyze the resulting carrier distributions to demonstrate our approach. The steady state is defined as the condition in which the current flow remains constant in both time and position under illumination and/or applied bias. In numerical simulations of electronic devices, the steady-state distributions of carrier concentration and electric potential are governed by the continuity equation, Poisson's equation, and Equation (1). The constitutive equation for carrier k is given by

$$-\frac{\partial j_k}{\partial x} - U_k(x) + G(x) = \frac{\partial n_k}{\partial t} = 0 \quad (9)$$

where $U_k(x)$ is the recombination rate for carrier k . Poisson's equation is given by

$$\frac{\partial}{\partial x} \left(\epsilon \epsilon_0 \frac{\partial \Psi}{\partial x} \right) = -q \left(n_h - n_e + n_D^+ - n_A^- + \frac{\rho_{\text{def}}}{q} \right) \quad (10)$$

where ϵ_0 is the permittivity of the vacuum, ϵ is the relative permittivity of the semiconductor, Ψ is the electrostatic potential, n_D^+ and n_A^- represent the concentrations of positive and negative charges resulting from ionized donor-like and acceptor-like defect states, respectively, and ρ_{def} is the total charge associated with other defects, assuming that any defect is nondegenerate. Moreover, in the case of one-dimensional solar cells, the total current density—the sum of electron and hole contributions at each position—must remain constant:

$$\frac{\partial(j_e + j_h)}{\partial x} = 0 \quad (11)$$

Otherwise, the charge balance among generation, recombination, and flow would be disrupted, leading to a loss of steady state.

The steady state is initiated by carrier generation that begins abruptly when a solar cell is illuminated. The system subsequently settles into a steady state, accompanied by carrier redistribution. In transport theory, there are two distinct modes of charge-carrier transport, each with a different driving force: drift and diffusion. This model represents a simplified expression of Boltzmann transport theory for charged particles that behave like an ideal gas. Drift is the transport driven by the electric field, while diffusion is governed by the gradient of the chemical potential of the particles, given by

$$u_{k,\text{dri}} = M_k n_k E = -\frac{M_k n_k \partial z_k q \Psi}{q} \quad (12)$$

and

$$u_{k,\text{diff}} = -D_k \text{grad } n_k = -\frac{M_k n_k \partial \mu_k}{q} \quad (13)$$

where E is the electric field and μ_k is the chemical potential of particle k . Einstein's relation, $D_k = M_k k T / q$, is assumed to derive the diffusion coefficients D_k . Since the electrochemical potential consists of the chemical potential and the electric potential, these equations can be derived from Equation (1). Because these movements continuously modify their own driving forces through Equation (10), tracking the entire transient evolution until steady state would, in principle, be required. Nevertheless, our primary aim here is to identify the factors that ultimately characterize the steady-state carrier distribution. To this end, we examine two key aspects: (i) the initial equilibrium state in the dark and (ii) the modulation that drives the system to reach short-circuit conditions. From the transport expressions in Equations (12) and (13), it is evident that, immediately after illumination, photo-generated carriers are influenced by both the built-in electric field and the carrier concentration (chemical potential) gradient present in the dark. We thus investigate these two influences under aspect (i). On the other hand, assuming spatially constant mobility, substituting Equation (1) into the continuity equation (Equation (9)) yields

$$\frac{\partial}{\partial x} \left(q z_k n_k \frac{\partial E_{F,k}}{\partial x} \right) = \frac{G(x) - U_k(x)}{M_k} \quad (14)$$

where the right hand side can be interpreted as the illumination-induced modulation, with the mobility M_k appearing as a scaling

factor of the net generation rate $G(x) - U(x)$. If M_k were infinite, changes in carrier concentration and electric field under short-circuit conditions would vanish, remaining identical to their dark-state values, and recombination would not occur. In this work, we therefore focus on the generation rate as a representative modulation component, which we defined as aspect (ii). The influence of each variable is quantified in the following sections using numerical simulation. All simulation input parameters are listed in Section 5.

3 | Results and Discussion

3.1 | Influence of the Initial Equilibrium State

To clarify how the redistribution of photogenerated carriers is influenced by the initial equilibrium state, we first examine five model systems that share an identical built-in electric field but differ in their carrier concentrations under dark conditions. These cases are constructed using five hypothetical combinations of dopant concentrations (N_d), effective density of states (N_{eff}), and the relative permittivity (ϵ), as listed in Table 1. Several of the N_{eff} and ϵ values are intentionally nonpractical and introduced solely to realize the target condition of a constant electric field. All other conditions follow Table 2 in Section 5. For clarity, a uniform generation rate of $1.03 \times 10^{21} \text{ cm}^{-3} \text{ s}^{-1}$ is applied throughout the $2 \mu\text{m}$ solar cell, corresponding to the AM1.5 photon flux above 1.4 eV.

Figure 1a,b shows the electric fields and carrier distributions in the dark, respectively. As intended, the electric fields are identical for all N_d values, whereas the carrier densities differ by several orders of magnitude. Thus, immediately after illumination the excess carriers experience the same drift driving force but different diffusion-force magnitudes. More precisely, the driving force for diffusion corresponds to the gradient of chemical potential, as shown in Equation (13). Figure 1c confirms that the equilibrium chemical potentials are identical, yet the different N_{eff} values modify the increment in chemical potential created upon illumination, leading to different diffusion forces.

Figure 2a shows the carrier distributions under short-circuit conditions. To improve clarity, the excess electron and hole concentrations—defined as the differences in carrier concentration between illuminated and dark conditions—are shown in Figure 2b,c, respectively. Here, we observe that the excess carrier distributions are almost identical across the various conditions, except for the case with $N_{\text{eff}} = 10^{16} \text{ cm}^{-3}$. This suggests that

TABLE 1 | Input parameters used in the SCAPS-1D simulations presented in Figures 1 and 2.

$N_d (\text{cm}^{-3})$	$N_{\text{eff}} (\text{cm}^{-3})$	ϵ
10^{14}	10^{16}	10^{-1}
10^{15}	10^{17}	10^0
10^{16}	10^{18}	10^1
10^{17}	10^{19}	10^2
10^{18}	10^{20}	10^3

excess carrier concentration under short-circuit conditions corresponds more closely to the electric field rather than the carrier distribution in the dark. If the steady-state excess carrier concentration were governed primarily by the carrier distribution in the dark, variations in N_d would lead to discernible differences in the excess carrier profile. However, this does not imply that redistribution is governed solely by drift; rather, it arises from the combined effect of both drift and diffusion.

The individual minority- and majority-carrier profiles clarify that drift and diffusion cooperate to produce the field-correlated excess carrier distribution observed in Figure 2b,c. The excess electron density in the p-type (Figure 2b) decreases monotonically toward the junction. Immediately after uniform photogeneration begins, the excess carrier concentration is much higher than the minority-carrier concentration in the dark; the diffusion term (Equation (13)) is negligible, while the electric field—which is the strongest at the junction (Figure 1)—drives electrons into the n-type region. This drift subsequently enhances diffusion in the same direction, and the trend persists until a steady state is reached. By comparison, the excess holes in the p-type region (Figure 2c)—representing excess majority carriers—behave differently. Uniform generation flattens the chemical-potential gradient that initially balanced the electric field, thereby weakening diffusion; drift is therefore dominant. The resulting profile becomes nonmonotonic, controlled by the interplay of drift and the residual diffusion.

We have demonstrated that the interplay of drift and diffusion unexpectedly yields steady-state excess carrier distributions that closely mirror the electric-field profile. While Equation (11) defines the steady state, it does not ensure a one-to-one correspondence between the electric-field and chemical-potential gradients, and the resulting excess carrier distribution. Figure 2d shows the chemical potential under short-circuit conditions, while Figure 2e,f show the gradients of chemical potential of electrons and holes, respectively. The two gradients are clearly non-identical; yet in the same regions, the electric field remains nearly identical.

Exceptionally, Figure 2b,c shows that, for the case with $N_{\text{eff}} = 10^{16} \text{ cm}^{-3}$, the excess carrier concentration near the contact is noticeably lower than in the other cases. The origin is a light-induced modification of electric field, known as a photovoltaic effect [33]. As Figure 2b,c indicates, the excess net charge—defined as the difference between the excess electron and excess hole concentrations—near the contacts is similar across all cases, while the charge from ionized dopants is negligible because this region is located outside the depletion layer. To keep the built-in field identical across the cases, a low ϵ was assigned to the low- N_{eff} (and thus a low- N_d) case, as shown in Table 1. Under such a low ϵ , a given excess charge produces a larger built-up field according to Equation (10). In the $N_{\text{eff}} = 10^{16} \text{ cm}^{-3}$ scenario, this built-up field near the contacts becomes comparable to the built-in field. During the transition toward a steady state, photogenerated carriers accumulate near the contacts, which strengthens the local field and accelerates carrier extraction by drift processes. Consequently, the steady-state excess carrier concentration in this region is lower than in the higher- N_{eff} cases. From a rigorous standpoint that includes the light-induced built-up electric field, the steady-state excess carrier distribution correlates not with the original built-in field but with

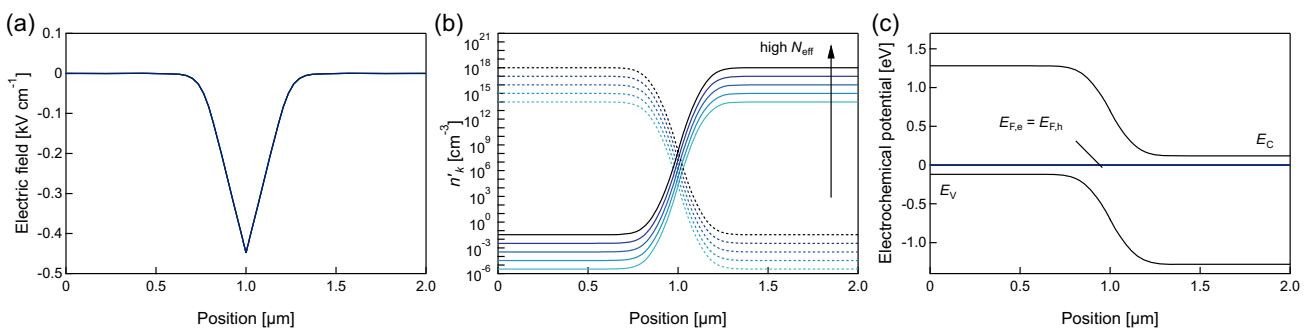


FIGURE 1 | Simulated (a) electric-field profile, (b) electron/hole concentrations, and (c) quasi-Fermi level (electrochemical potential) for the homo-pn solar cell under dark conditions. The effective density of states, dopant concentration, and relative permittivity were adjusted so that all cases exhibit the same built-in electric field.

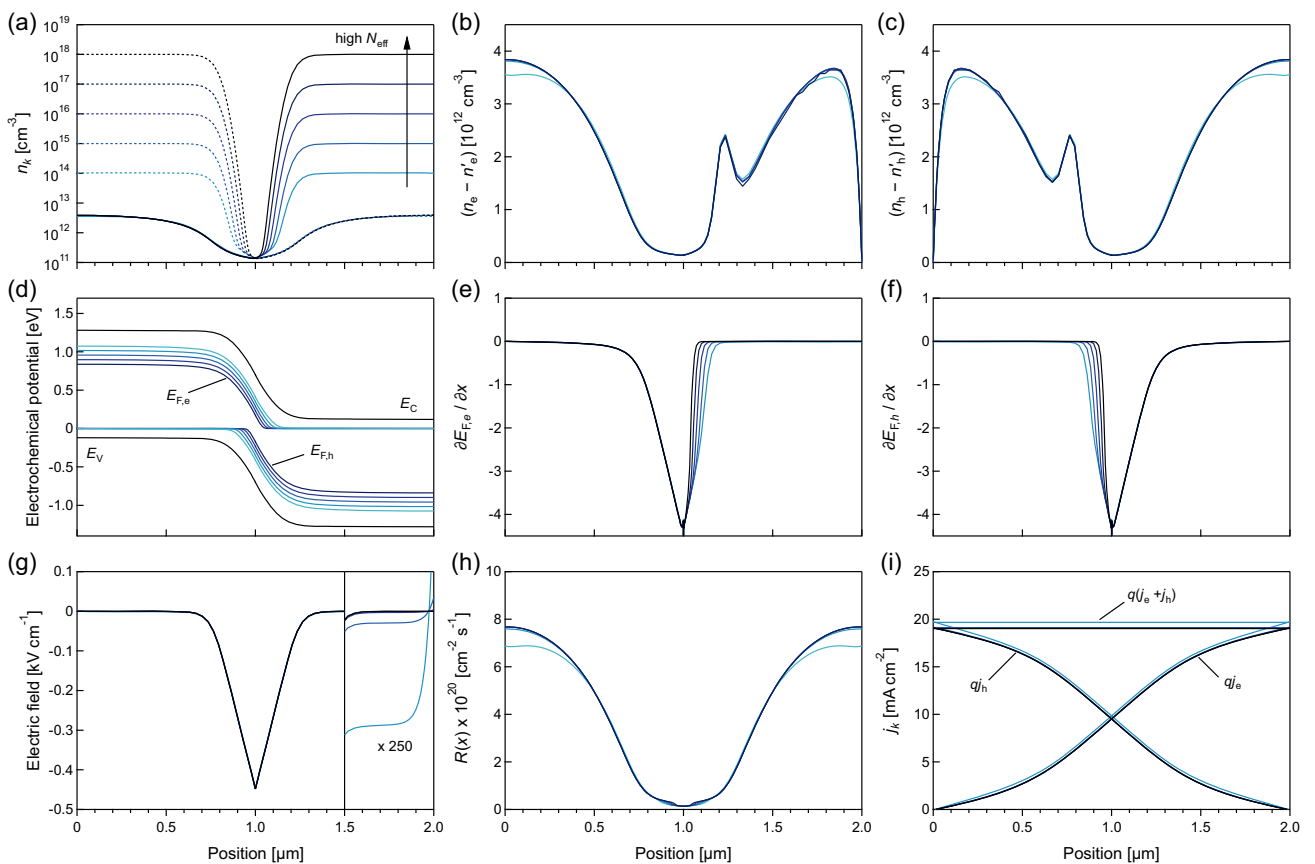


FIGURE 2 | Simulated steady-state profiles under short-circuit conditions for model cells sharing the same internal electric field: (a) electron and hole concentrations; (b) excess electron and (c) excess hole concentrations; (d) electron and hole quasi-Fermi levels; (e) spatial gradient of the electron quasi-Fermi level and (f) that of the hole quasi-Fermi level; (g) steady-state electric-field profile (vertical axis magnified $\times 250$ in the 1.5–2.0 μm); (h) Shockley–Read–Hall recombination-rate profile; (i) electron, hole and total current-density profiles.

the built-up field under steady-state conditions. Indeed, a numerical study has even shown that a device with no built-in electric field can operate as a solar cell [5]. Although the reference provides only the band diagram at the maximum-power point, the most plausible explanation for the presence of J_{SC} is the formation of a built-up electric field under illumination, with the excess carrier distribution adjusting so that the net current in Equation (6) becomes positive. Even at the maximum-power point, this built-up field is directed opposite to the photocurrent, yet it uniquely characterizes the excess carrier profile: the minority-carrier concentration decreases as the built-up field increases.

In Figure 2h, the spatial profile of the recombination rate is identical for all cases except the $N_{\text{eff}} = 10^{16} \text{ cm}^{-3}$ device, where the lower excess carrier concentration near the contacts suppresses recombination. Figure 2i shows the electron- and hole-current densities together with their sum. The same recombination rate corresponds to the same current density, which reflects the charge balance described by Equation (6). This observation stems from the fact that the excess minority-carrier distributions remain almost identical across the scenarios (Figure 2b,c). When the majority-carrier density exceeds the minority-carrier density, the recombination rate is proportional to the excess

minority carrier concentration. Thus, increasing the steady-state electric field in regions with significant recombination effectively suppresses J_{SC} losses, as in the $N_{eff}=10^{16} \text{ cm}^{-3}$ scenario; the strong electric field near the contacts suppresses recombination, resulting in a higher short-circuit current density. Therefore, evaluating and controlling the built-up electric field under short-circuit conditions is essential to enhance carrier separation efficiency by tailoring the excess carrier distribution.

3.2 | Influence of the Generation-Rate Profile

In this section, we examine the influence of generation rate, acting as the trigger for a steady state, on the excess-carrier distribution and its relation to the electric field. We begin with a constant generation rate and quantify the resulting steady-state profiles. The insights obtained here provide fundamental knowledge for the next section, where we investigate a more realistic generation profile—namely, an exponentially decaying profile.

To systematically investigate the effect of generation-rate distribution on the excess-carrier distribution, we introduce a spatially localized, constant generation rate. This approach elucidates the relationship between the generation rate and the distribution of the electric field without the influence of spatial variations of generation rates, providing an essential insight into the analysis of the practical generation profile discussed in Section 3.3. We assume a linear relationship between the excess-carrier concentration and the generation rate. In words, the excess-carrier distribution produced by the sum of segmented generation rates equals the sum of the profiles calculated for each rate separately. This linearity holds when the recombination rate is proportional to the minority-carrier concentration and the photovoltaic effect is negligible, as in the present system. Verification of this linear relationship is provided in the Supporting Information.

The solar cell examined here, with $N_{eff}=10^{18} \text{ cm}^{-3}$ and $N_d=10^{16} \text{ cm}^{-3}$, is the same as that presented in Section 3.1. As shown in Figure 3a, the generation rate was fixed at $1.03 \times 10^{21} \text{ cm}^{-3} \text{ s}^{-1}$ within five 0.2 μm -wide segments (0–0.2, 0.2–0.4, 0.4–0.6, 0.6–0.8, and 0.8–1.0 μm), forming a boxcar-shaped spatial profile. Since the device under consideration is a homo-*pn* junction, only the generation rate within the *p*-type region was considered.

Figure 3b illustrates how varying spatial generation distributions affect the excess-electron concentration. Although the total generation rate is identical in all segments, the distribution profile and the total amount of excess electrons vary depending on the generation position. In the *p*-type region, the peak position of the excess-electron concentration aligns with generation site, and the maximum concentration decreases as the generation region approaches the *pn* junction. In other words, in regions with stronger electric fields, excess carriers are less likely to remain where they are generated, even when the generation rate is the same. This trend can be attributed to enhanced drift transport driven by stronger electric fields during the transient process leading to a steady state. Therefore, to suppress the peak excess-carrier concentration in photogeneration regions—which serves as the reactant for recombination in Equations (7) and (8)—the internal electric field must be strengthened.

Notably, a significant tail in the excess-electron concentration is observed extending beyond the generation regions. This clearly indicates that, as discussed in Section 3.1, the transition from dark to short-circuit conditions involves both drift and diffusion processes. Immediately after photogeneration confined to a specific region within the *p*-type layer (e.g., 0.4–0.6 μm), the generated electrons diffuse into both adjacent regions where no generation occurs. Since the electron concentration in the dark is sufficiently low, it has negligible influence on the diffusion

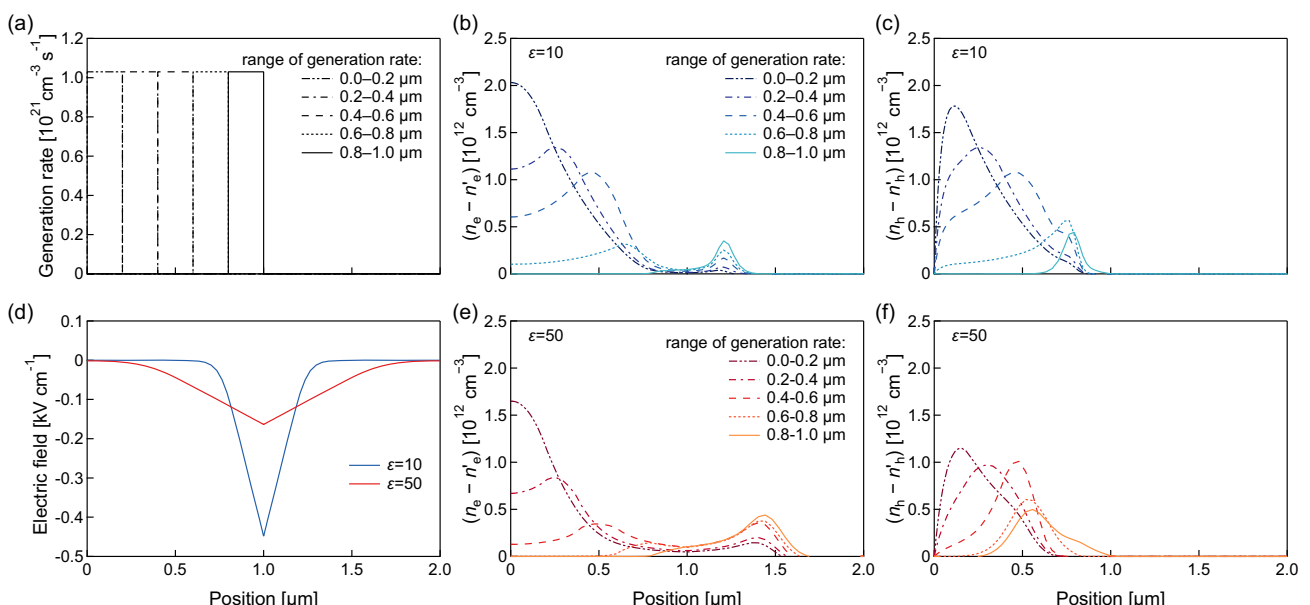


FIGURE 3 | (a) Input generation-rate profiles spatially localized within 0.2 μm -wide segments (0–0.2, 0.2–0.4, 0.4–0.6, 0.6–0.8, and 0.8–1.0 μm). (b) Excess-electron and (c) excess-hole concentrations for a device with relative permittivity $\epsilon = 10$ under short-circuit conditions. (d) Built-in electric fields for $\epsilon = 10$ and 50. (e) Excess-electron and (f) excess-hole concentrations for the otherwise identical device with $\epsilon = 50$; the broader steady-state electric-field profile responsible for these changes is shown in (d).

driving force. In contrast, the built-in electric field driving electrons toward the *n*-type region (right-side direction in our model) is stronger near the *pn* junction. Consequently, the net driving force to the left is weakened, whereas that to the right is enhanced through drift transport, resulting in a longer tail on the left and a shorter, sharper tail on the right due to the reduction of the apparent excess carrier concentration. For example, when the generation occurs in the 0.0–0.2 μm region, the tail accounts for 49.7% of the total excess carrier concentration in the *p*-type region. In other words, a number of excess carriers comparable to those generated locally appears as a tail in regions without generation. Such a tail, despite appearing in a region with zero generation rate, still contributes to recombination in the same way as the peak excess-carrier concentration. Therefore, suppressing these tails is essential for minimizing recombination losses.

In contrast, the *n*-type region exhibits different behavior. The excess-electron concentration (i.e., the majority carrier) shows a local maximum at approximately 1.2 μm, despite the absence of carrier generation in this region. This accumulation appears as a tail far from the generation site, and the location of the maximum is largely independent of the generation position. The number of accumulated electrons (i.e., the concentration peak) in this region becomes more pronounced when the generation occurs closer to the *pn* junction. This indicates that carrier generation occurring closer to the junction has a greater influence on the excess electron distribution within the *n*-type layer.

Figure 3c shows that the excess-hole distribution with different generation profiles exhibits three prominent features. First, the maximum excess-carrier concentration appears at the generation site. Similar to the excess electrons in the *p*-type region, the maximum value decreases as the generation location approaches the *pn* junction due to the distribution of the electric field. Tails are also observed in these distributions. Second, a distinct local accumulation is observed around 0.8 μm, similar to the behavior of electrons in the *n*-type region. Third, diffusion of holes into the *n*-type region is negligible.

The electric field plays a crucial role in regions near the *pn* junction, as discussed in Section 3.1. Figure 3e,f shows the impacts of a broader electric-field profile on the excess-electron and excess-hole distributions, respectively. The broader electric field was obtained using $\epsilon = 50$, as shown in Figure 3d. In the *p*-type layer, when the generation occurs in 0.0–0.8 μm, the excess-electron concentration for $\epsilon = 50$ is lower than that for $\epsilon = 10$. This is because the electric field in this region is stronger for $\epsilon = 50$. In contrast, when the generation position is at 0.8–1.0 μm, the opposite trend is found. Furthermore, the accumulation in the *n*-type region occurs around 1.45 μm, which is farther away from the *pn* junction compared with the previous condition. In Figure 3f, similar features are also observed in the excess-hole distribution, including the influence of the electric field and the shift in the accumulation position.

In summary, systematic simulations revealed that the overall excess-carrier profile consists of the carrier generation at specific positions and the transport across neighboring regions, with the internal electric field emerging as a decisive factor. Both the local peak and the extended tail of the excess carrier concentration

diminish as the electric field strengthens, yet each contributes to recombination, regardless of the presence of generation. This highlights that recombination is not limited to regions with carrier generation. As discussed in Section 3.1, the overall excess-carrier concentration, including both the generation and the transport, is characterized by the steady-state electric field. Therefore, it is necessary to design the built-up electric field in accordance with the actual generation-rate profile to control the excess-carrier concentration in both generation and nongeneration regions.

3.3 | Exponential Generation

In practical solar cells, the generation-rate profile is seldom uniform; it usually decays exponentially from the illuminated surface, and advanced architectures—heterojunction [11, 34–37], multijunction [38–41], back reflectors [42], or bandgap grading [15]—can render it more complex. An exponential profile, therefore, remains a useful model for capturing the essential inhomogeneity of carrier generation. As discussed in the previous section, which showed that the locations of generation rate and electric field strongly shape the excess-carrier distribution, we now analyze the influence of inhomogeneous generation profiles, together with the electric field, on the steady-state carrier distributions and recombination rates.

The solar cell design used was identical to that described in Section 3.2. The dielectric constant was primarily set to $\epsilon = 10$. The *p*-type layer was designed as the sole absorber, whereas the *n*-type layer is treated as optically transparent. The absorption coefficient α in the *p*-type region was calculated with the E_g -sqrt model implemented in SCAPS, that is, $\alpha \propto (\hbar\omega - E_g)^{1/2}$. To examine the influence of the generation-rate distribution, we also simulated a case in which the absorption coefficient was reduced to half its default value, keeping all other parameters fixed. In both cases, a 1 μm-thick *p*-type layer absorbs all above-gap photons.

Figure 4 shows the simulated generation-rate profiles for solar cells with different absorption coefficients in the *p*-type layer, irradiated from the *n*-type surface under the AM1.5 solar

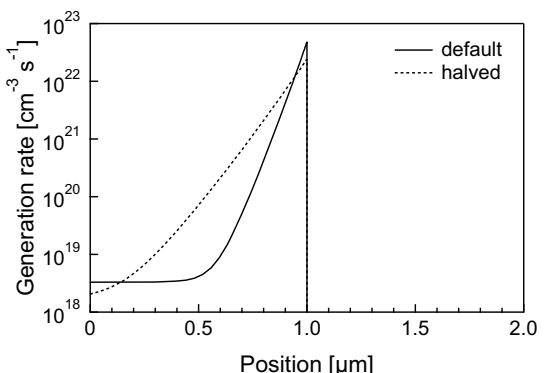


FIGURE 4 | Generation rates for solar cells comprising a *p*-type layer with either the default absorption coefficient or half of that value, and a transparent *n*-type layer, illuminated from the *n*-type surface under an AM1.5 solar spectrum.

spectrum. Additionally, following the approach in Section 3.2, spatially segmented generation rates were considered as well. To capture the steep variation near the *pn* junction, the generation region was divided into five segments—0.0–0.6, 0.6–0.7, 0.7–0.8, 0.8–0.9, and 0.9–1.0 μm—which were used in the simulations.

Figure 5a,b shows the excess-electron and excess-hole distributions, respectively, obtained by applying different segments of an exponential generation rate. Note that the vertical axis of the excess-electron concentration in the *p*-type region is magnified for clarity. The curves may appear separated at 1.0 μm, but it is in fact a single continuous curve. Due to the exponential nature of the generation rate, the excess-carrier concentration profile deviates significantly from that obtained under a uniform generation rate, as shown in Figure 3. In Figure 5a, the maximum excess-electron concentration of each segment in *p*-type region increases as the location approaches the *pn* junction, overcoming the influence of the increasing electric field. Notably, carriers generated in the 0.8–0.9 and 0.9–1.0 μm regions exhibit almost no tail on the contact side, whereas carriers generated in other regions display tails, though of small magnitude. In the *n*-type region, substantial accumulations of electrons are observed, with their concentration significantly higher than in the *p*-type region. This behavior arises from the exponential generation profile, which concentrates carrier generation near the illuminated surface. Before reaching the steady state, electrons generated in the *p*-type layer do not accumulate there but are instead swept by the electric field and collected in the *n*-type region. On the other hand, as shown in Figure 5b, the excess-hole distribution is predominantly an accumulation component in the *p*-type region and is scarcely present in the *n*-type region.

Figure 5c illustrates the distribution of the recombination rate, which occurs predominantly in the *p*-type region and is nearly absent in the *n*-type region, reflecting the distribution of excess-minority carriers. The sharp peak near the interface is primarily due to carriers generated in the 0.8–1.0 μm region. In contrast, the broad recombination observed deeper in the *p*-type is due to carriers generated in the 0.0–0.7 μm range. Compared to the case with a uniform generation rate in the *p*-type region shown in Figure 2e, the overall recombination is lower except in the immediate vicinity of the *pn* junction. This indicates that the high generation rate near the *pn* junction is well aligned with the internal electric field and therefore effectively suppresses recombination.

Building on the linear relationship between generation rate and excess-carrier concentration detailed in the Supporting Information, the total excess carrier concentration in Figure 5a,b can be regarded as the linear superposition of the excess-carrier profiles obtained from infinitesimally thin spatial slices of uniform generation. Furthermore, Section 3.1 shows that the shape of each slice-derived profile is governed by the electric field. Section 3.2 further reveals that this shape invariably consists of a peak within the generating region and a tail extending into nongenerating regions. The absolute magnitude of the generation rate merely scales this field-defined profile. For the uniform generation profile shown in Section 3.2, both the peak and the tail diminish in regions with strong electric field. An exponential generation profile, in contrast, redistributes the generation rate from deeper regions—where peaks and tails would otherwise be pronounced—toward the near *pn*-junction region, where the field is stronger and both features are suppressed. This redistribution moderates the overall excess-carrier distribution and consequently mitigates recombination losses.

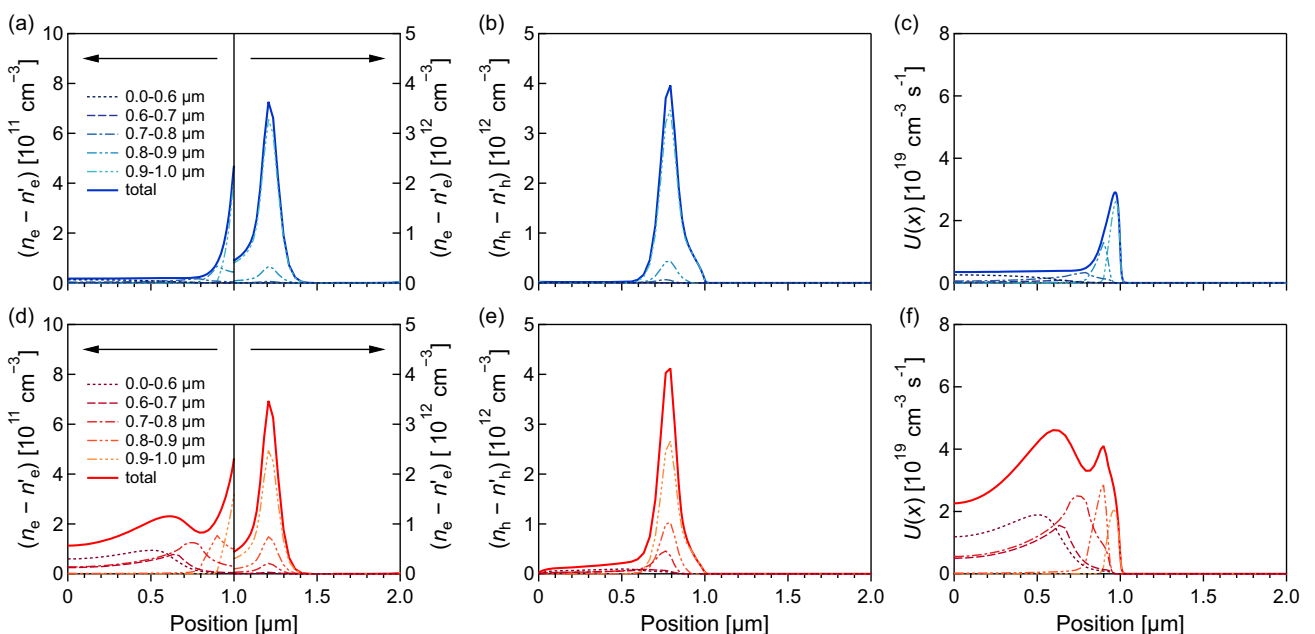


FIGURE 5 | Steady-state profiles obtained when an exponentially decaying generation rate is applied segment by segment. Panels (a–c) show excess-electron density, excess-hole density, and Shockley–Read–Hall (SRH) recombination rate, respectively the default absorption coefficient α . Panels (d–f) present the same three quantities for the halved absorption coefficient. For clarity, the ordinate of the excess electron plot in the *p*-type region is vertically magnified. Solid curves indicate the case in which the sum of each segmented generation is applied (no segmentation).

Figure 5d–f corresponds to Figure 5a–c but presents the results when the absorption coefficient is halved. Halving the absorption coefficient effectively redistributes photogeneration toward deeper regions, as noted above. As shown in Figure 4, the generation rate in the 0.9–1.0 μm region is reduced in halved α , resulting in decreased excess-electron concentration in that region, as shown in Figure 5d,e. Conversely, in the deeper region, the generation rate becomes higher than in the default case, leading to a correspondingly increased excess-carrier concentration. Additionally, the contribution of tail becomes more pronounced. In Figure 5e, excess electrons generated in the 0.6–0.7 and 0.7–0.8 μm regions exhibit extended tails that reach the left contact. Together, these tails account for more than half of the total excess-electron concentration in the 0.0–0.6 μm region, resulting in most of the recombination there originating from electrons generated in the 0.6–0.8 μm region, as shown in Figure 5f. Although the generation rate in the 0.0–0.8 μm region constitutes only 1.30% of the total, the recombination associated with these carriers contributes up to 85.7% of the total recombination. This reflects the fact that an excessive large portion of the photogeneration is assigned to deep region where the internal electric field is insufficient, thereby magnifying the influence of the carrier tails, as shown in Figure 3b. Although removing generation in the 0.9–1.0 μm range lowers the local excess carrier concentration, it provides no relief in the overall recombination rate.

In practical devices, the strength and width of the internal electric field must be matched to the photogeneration profile to minimize the excess-carrier concentration and, consequently, the recombination rate. To explore this dependence in isolation, we varied the dielectric constant ϵ from 1 to 100 while keeping the built-in potential fixed and calculated the resulting recombination profiles under short-circuit conditions.

Figure 6a presents a heat map of the electric field in the dark as functions of position and the dielectric constant ϵ . The dash-dotted contour marks where $|\text{electric field}| = 1 \text{ kV cm}^{-1}$; the region enclosed by this contour corresponds to the depletion layer. As ϵ increases, the depletion layer width x_D expands, and the maximum interfacial field E_{MAX} decreases. Figure 6b shows the corresponding heat map of the steady-state recombination rate, calculated using the E_g -sqrt-based absorption coefficient α shown in Figure 4 (the underlying carrier distributions are given in Figure S2 of the Supporting Information). Most recombination occurs on the *p*-type side, reflecting the excess-minority-carrier

profile shown in Figure 5a,b. Two high-recombination regions, labeled Region I and Region II, can be distinguished by dotted contours at 25% of the maximum recombination rate. Region I appears where the depletion layer is narrow, and recombination there is dominated by the long tails identified in Figure 5d. This region diminishes as x_D broadens and becomes negligible for $\epsilon > 3$ ($x_D > 0.4 \mu\text{m}$). Region II appears at larger ϵ and is driven by the photogeneration peak near the junction (see Figure 5b). When $\epsilon \leq 5.5$ ($E_{\text{MAX}} > 55 \text{ kV cm}^{-1}$), Region II diminishes. Taken together, these results indicate that a strong interfacial field is required to sweep out carriers generated near the junction. A dielectric-constant range of $3 < \epsilon < 5.5$ provides a balanced solution under the default α , avoiding both Region I and Region II.

Figure 6c shows the recombination heat map for the halved absorption coefficient. As photogeneration shifts deeper into the bulk, the area of Region I expands, and recombination suppression requires $x_D > 0.6 \mu\text{m}$. Simultaneously, the reduced generation peak at the junction lowers the threshold E_{MAX} for avoiding Region II to 18 kV cm^{-1} , thereby broadening the optimal electric field corresponding to dielectric-constant range to $7.3 < \epsilon < 53$.

Although the default absorption coefficient yields a lower total recombination rate (see Figure S2 in the Supporting Information for the total recombination and diode currents), in practical materials a larger α typically corresponds to a higher effective density of states and reduced mobility [43], which in turn increases the excess carrier concentration and thus the recombination rate. The analysis presented in Figure 6 remains valuable for assessing the role of the internal electric field given a specific generation rate profile rather than for comparing absolute recombination rates across different α values.

These insights are reflected in advanced solar-cell architectures. In Cu(In,Ga)(S,Se)₂ (CIGS) cells, for instance, a double bandgap grading is employed in which the Ga/(Ga+In) ratio increases toward both the *pn* junction and the back contact, thereby widening the local bandgap. While this grading is primarily designed to harvest long-wavelength photons and suppress back-surface recombination, it also reduces both the excess-carrier peak and tail, as observed in our findings. With a dielectric constant $\epsilon \sim 13$, a dopant concentration of $\sim 10^{16} \text{ cm}^{-3}$, and a front-grading width of $\sim 200 \text{ nm}$, the interfacial field in CIGS remains below 100 kV cm^{-1}

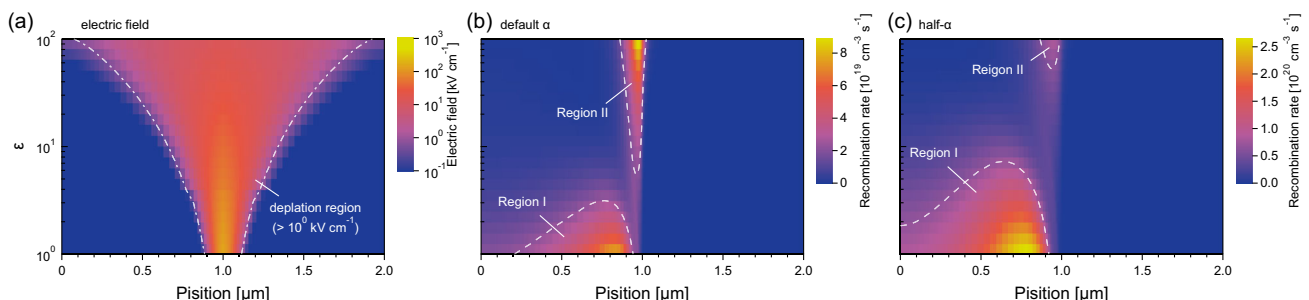


FIGURE 6 | (a) Heat map of the electric field magnitude in the dark as a function of position (horizontal axis) and relative dielectric constant ϵ (vertical axis, 1–100). Dash-dotted contour denotes $|\text{electric field}| = 1 \text{ kV cm}^{-1}$. The region enclosed by this contour corresponds to the depletion layer. Spatial distributions of the steady-state recombination rate under short-circuit conditions calculated using (b) default α and (c) a halved α . Dotted contours in (b and c) indicate 25% of the respective maximum recombination rate.

[44, 45] By contrast, if the absorber were CuInSe₂ (CIS, bandgap ~ 1 eV), its higher absorption coefficient would be expected to produce a more pronounced excess-carrier peak at the interface [46]. In CIGS, however, front grading up to 1.4 eV redistributes photogeneration deeper into the absorber, thereby suppressing the excess carrier-peak at the interface compared with the CIS case. The remaining photogeneration in deeper regions is then addressed by the back grading, which reduces the tail and bulk recombination, as well as recombination at the back contact.

In general, absorbers with high α require either a strong electric field near the surface or a high-quality interface with minimal defects, so that recombination remains low even at a high excess-carrier peak. Conversely, low- α materials demand doping or band-engineering schemes that create a broad internal field and reduce defect-mediated recombination, which is most likely to arise from carrier tails. Hence, the internal electric-field design must be tailored to the generation profile of the material and coordinated with defect-control strategies.

4 | Conclusion

This study establishes a clear physical perspective of carrier separation under short-circuit conditions in *homo-pn* junction solar cells by means of the charge-balance scheme and systematic SCAPS-1D simulations. Because the divergence of the current density equals the net generation, quantifying J_{SC} reduces to identifying the set steady-state excess carrier distributions. Using hypothetical systems in which the electric field is fixed while carrier concentration varies in the dark, we show that the steady-state carrier profile is determined by the internal electric field. Although the equilibrium carrier distribution in the dark does not affect the excess carriers, both drift and diffusion govern the transient pathway from equilibrium to the steady state. Segmented-generation analysis further confirms that the excess-carrier profile consists of not only a locally generated excess-carrier peak but also a tail transported from other regions. Combining this insight with the linear relationship between generation rate and excess-carrier density, we find that representing the overall excess-carrier landscape as a superposition of these peak and tail features offers a direct, quantitative route to J_{SC} . Applying the method to exponential generation profiles, as a realistic example, demonstrates how the absorption coefficient—together with field width and strength—jointly suppresses peaks and tails. Future extensions will incorporate spatially varying trap distributions and band-offset effects to extend the framework toward realistic solar cells.

5 | Simulation Details

Numerical simulations are valuable tools for analyzing device performance. In this work, we employed SCAPS-1D, a specialized device simulator for solar cells developed by Burgelman et al. [29] to investigate steady-state carrier distributions. The calculations are based on the continuity equations for electrons and holes, as well as Poisson's equation. These coupled equations

TABLE 2 | Input parameters for SCAPS-1D.

Parameters	Values
Thickness of each layer (μm)	1
Electron affinity, χ (eV)	4.28
Bandgap, E_g (eV)	1.4
Dopant density, N_d (cm^{-3})	$10^{14}\text{--}10^{20}$
Effective density of states, N_{eff} (cm^{-3})	$10^{14}\text{--}10^{20}$
Electron mobility ($\text{cm}^2 \text{ V}^{-1} \text{ s}^{-1}$)	10^2
Hole mobility ($\text{cm}^2 \text{ V}^{-1} \text{ s}^{-1}$)	10^2
Relative dielectric constant	$10^{-3}\text{--}10^3$
Surface recombination velocity for majority carriers (cm s^{-1})	10^7
Surface recombination velocity for minority carriers (cm s^{-1})	10^2
Trap density, N_t (cm^{-3})	2×10^{14}
Capture cross-section, σ (cm^{-2})	10^{-13}
Trap level from the vacuum level (eV)	4.98

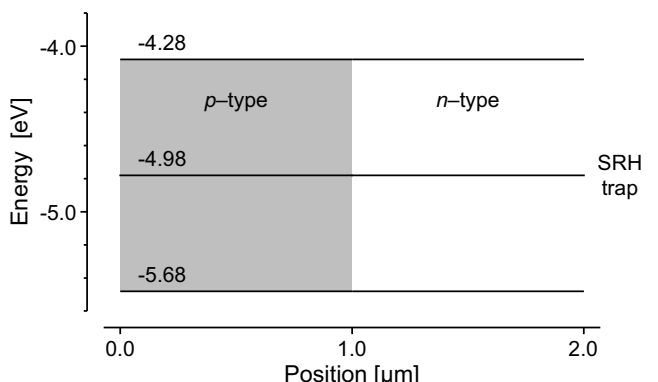


FIGURE 7 | Schematic band diagram of the *homo-pn* junction solar-cell setup in the device simulator.

are solved using the Gummel–iteration scheme with Newton–Raphson substeps. A classical drift-diffusion model was adopted, neglecting quantum transport effects.

We consider hypothetical *homo-pn* solar cells. N_d denotes the acceptor concentration for *p*-type layers and the donor concentration for *n*-type layers. The effective density of states N_{eff} was set to the same value in the conduction and valence bands to preserve the *homo-pn* junction. The input parameters are listed in Table 2, and the band diagram is shown in Figure 7. These parameters were primarily obtained from the literature [47], with particular reference to CdTe solar cells. In our model, the bandgap of *p*- and *n*-type layers, E_g , was set to 1.4 eV. We also included uniform Shockley–Read–Hall (SRH) defects as the primary recombination mechanism [27, 28]. The capture cross sections for electrons and holes, σ , the trap density, N_t , and the trap level from vacuum level were 10^{-13} cm^{-2} , $2 \times 10^{14} \text{ cm}^{-3}$, and 4.98 eV, respectively. The trap level corresponds to the midgap in the absorber. The surface recombination velocities

for majority and minority carriers were set to 10^7 and 10^2 cm s^{-1} , respectively.

Acknowledgments

This work was supported by JST SPRING (No. JPMJSP2110), JSPS KAKENHI (Nos. 23K26432 and 24KJ1392), and Collaborative Research Project of Materials and Structures Laboratory, Institute of Integrated Research, Institute of Science, Tokyo.

Conflicts of Interest

The authors declare no conflicts of interest.

Data Availability Statement

Research data are not shared.

References

- P. Würfel and U. Würfel, *Physics of Solar Cells: From Basic Principles to Advanced Concepts*, (Wiley-VCH, 2009).
- S. J. Fonash, *Solar Cell Device Physics 2nd ed.*, (Academic Press, 2010).
- K. W. Böer, *Handbook of the Physics of Thin-Film Solar Cells* (Springer Berlin, 2013).
- J. Nelson, *The Physics of Solar Cells* (Imperial College Press, 2003).
- U. Würfel, A. Cuevas, and P. Würfel, *IEEE Journal of Photovoltaics* 5 (2015): 461.
- R. Brendel and R. Peibst, *IEEE Journal of Photovoltaics* 6 (2016): 1413.
- E. T. Roe, K. E. Egelhofer, and M. C. Lonergan, *ACS Applied Energy Materials* 1 (2018): 1037.
- U. Rau and T. Kirchartz, *Advanced Materials Interfaces* 6 (2019): 1900252.
- W. Shockley and H. J. Queisser, *Journal of Applied Physics* 32 (1961): 510.
- H. Lin, M. Yang, X. Ru, et al., *Nature Energy* 8 (2023): 789.
- K. Yoshikawa, H. Kawasaki, W. Yoshida, et al., *Nature Energy* 2 (2017): 17032.
- T. Xue, B. Fan, K.-J. Jiang, et al., *Energy & Environmental Science* 17 (2024): 2621.
- D. Xu, M. Wu, Y. Bai, et al., *Advanced Functional Materials* 35 (2025): 2412946.
- P. Jackson, R. Wuerz, D. Hariskos, E. Lotter, W. Witte, and M. Powalla, *Physica Status Solidi RRL* 10 (2016): 583.
- M. Nakamura, K. Yamaguchi, Y. Kimoto, Y. Yasaki, T. Kato, and H. Sugimoto, *IEEE Journal of Photovoltaics* 9 (2019): 1863.
- J. Keller, K. Kiselman, O. Donzel-Gargand, et al., *Nature Energy* 9 (2024): 467.
- B. M. Kayes, H. Nie, R. Twist, et al., *Proceedings of the 37th IEEE Photovoltaic Specialists Conference* (2011), 000004.
- R. Mallick, X. Li, C. Reich, et al., *IEEE Journal of Photovoltaics* 13 (2023): 510.
- W. K. Metzger, D. W. Miller, R. Mallick, et al., *IEEE Journal of Photovoltaics* 12 (2022): 1435.
- C. Yan, J. Huang, K. Sun, et al., *Nature Energy* 3 (2018): 764.
- X. Cui, K. Sun, J. Huang, et al., *Energy & Environmental Science* 12 (2019): 2751.
- J. Zhou, X. Xu, H. Wu, et al., *Nature Energy* 8 (2023): 5.
- Q. Zhao, R. Tang, B. Che, et al., *Advanced Materials* 37 (2025): 2414082.
- T. Kuwano, R. Katsume, K. Kazumi, and Y. Nose, *Solar Energy Materials and Solar Cells* 221 (2021): 110891.
- I. Sumiyoshi and Y. Nose, *Journal of Applied Physics* 133 (2023): 235702.
- U. Rau, G. Kron, and J. H. Werner, *The Journal of Physical Chemistry B* 107 (2003): 13547.
- P. Würfel, *Physica E: Low-Dimensional Systems and Nanostructures* 14 (2002): 18.
- X. Zhang, Z. K. Yuan, and S. Chen, *Solar RRL* 3 (2019): 1900057.
- M. Burgelman, P. Nollet, and S. Degrave, *Thin Solid Films* 361–362 (2000): 527.
- Y. Zhou and G. Long, *Journal of Physical Chemistry C* 121 (2017): 1455.
- T. Minemoto, T. Matsui, H. Takakura, et al., *Solar Energy Materials and Solar Cells* 67 (2001): 83.
- S. Akel, A. Kulkarni, U. Rau, and T. Kirchartz, *PRX Energy* 2 (2023): 013004.
- H. Takeuchi, Y. Kamo, Y. Yamamoto, T. Oku, M. Totsuka, and M. Nakayama, *Journal of Applied Physics* 97 (2005): 063708.
- A. G. Aberle, *Progress in Photovoltaics: Research and Applications* 8 (2000): 473.
- M. Taguchi, A. Yano, S. Tohoda, et al., *IEEE Journal of Photovoltaics* 4 (2014): 96.
- D. Adachi, J. L. Hernández, and K. Yamamoto, *Applied Physics Letters* 107 (2015): 233506.
- M. Taguchi, K. Kawamoto, S. Tsuge, et al., *Progress in Photovoltaics: Research and Applications* 8 (2000): 503.
- E. Aydin, E. Ugur, B. K. Yildirim, et al., *Nature* 623 (2023): 732.
- X. Y. Chin, D. Turkay, J. A. Steele, et al., *Science* 381 (2023): 59.
- L. Xu, J. Lium F. Toniolo, M. D. Bastiani, et al., *ACS Energy Letters* 7 (2022): 2370.
- L. Mazzarella, Y. H. Lin, S. Kirner, et al., *Advanced Energy Materials* 9 (2019): 1803241.
- A. Cordaro, R. Müller, S. W. Tabernig, et al., *ACS Photonics* 10 (2023): 4061.
- T. Kirchartz and U. Rau, *Sustainable Energy & Fuels* 2 (2018): 1550.
- T. Dullweber, G. Hanna, W. S. Kolahi, et al., *Thin Solid Films* 361–362 (2000): 478.
- A. L. Sampietro, K. Yoshida, S. Wang, et al., *Solar Energy Materials and Solar Cells* 223 (2021): 110948.
- J. E. Jaffe and A. Zunger, *Physical Review B* 29 (1984): 1881.
- K. O. Hara and N. Usami, *Journal of Applied Physics* 114 (2013): 153101.

Supporting Information

Additional supporting information can be found online in the Supporting Information section. **Figure S1.** Cumulative plots for each profile shown in Figure 3. (a) excess-electron and (b) excess-hole concentrations for the device with relative permittivity $\epsilon = 10$; colored curves correspond to the five individual boxcar segments (0.0–0.2, 0.2–0.4, 0.4–0.6, 0.6–0.8, 0.8–1.0 μm). The dotted curve shows the profile calculated for the sum of the five generation profiles, and the black curve plots the residual. Panels (c) and (d) repeat the analysis for a device with a broader electric field realized by $\epsilon = 50$. **Figure S2.** Heat maps of the steady-state excess-

carrier distributions and recombination currents under short-circuit conditions, plotted versus position (horizontal axis) and dielectric constant ϵ (vertical axis). Panels (a) and b) show the excess-electron and excess-hole concentrations, respectively, for the case using the default absorption coefficient, corresponding to the recombination rate maps in Figures 6a and 6b of the main text. Panel (c) shows the total bulk-recombination current density (r) defined by Equation (6), together with the surface-recombination current density at the p-type side contact, $v_1(n_e - n'_e)$ and that at the n-type side contact, $v_2(n_h - n'_h)$. The sum of surface-recombination current densities gives the total diode current density. Panels (d-f) present, in the same order, the excess-electron concentration, excess-hole concentration, and recombination current density curves obtained when the absorption coefficient is halved.